IMAGING METHODOLOGY - Rapid Communication

Magnetic Resonance in Medicine 74:925–933 (2015)

Diffusion MRI with Concurrent Magnetic Field Monitoring

Bertram J. Wilm,[1]* Zoltan Nagy,[2] Christoph Barmet,[1,3] S. Johanna Vannesjo,[1] Lars Kasper,[1,4] Max Haeberlin,[1] Simon Gross,[1] Benjamin E. Dietrich,[1] David O. Brunner,[1] Thomas Schmid,[1] and Klaas P. Pruessmann[1]

Purpose: Diffusion MRI is compromised by unknown field perturbation during image encoding. The purpose of this study was to address this problem using the recently described approach of concurrent magnetic field monitoring.

Methods: Magnetic field dynamics were monitored during the echo planar imaging readout of a common diffusion-weighted MRI sequence using an integrated magnetic field camera setup. The image encoding including encoding changes over the duration of entire scans were quantified and analyzed. Field perturbations were corrected by accounting for them in generalized image reconstruction. The impact on image quality along with geometrical congruence among different diffusion-weighted images was assessed both qualitatively and quantitatively.

Results: The most significant field perturbations were found to be related to higher-order eddy currents from diffusion-weighting gradients and B_0 field drift as well as gradual changes of short-term eddy current behavior and mechanical oscillations during the scan. All artifacts relating to dynamic field perturbations were eliminated by incorporating the measured encoding in image reconstruction.

Conclusion: Concurrent field monitoring combined with generalized reconstruction enhances depiction fidelity in diffusion imaging. In addition to artifact reduction, it improves geometric congruence and thus facilitates image combination for quantitative diffusion analysis. **Magn Reson Med 74:925–933, 2015. © 2015 Wiley Periodicals, Inc.**

Key words: diffusion; DWI; DTI; artifact correction; distortion correction; field monitoring

INTRODUCTION

Diffusion-weighted (DW) MR (1) and MRI (2) allows for a noninvasive assessment of water diffusion, thereby enabling probing of the tissue microstructure. DW imaging (DWI) is a standard method for the early detection of stroke (3), and the structural information from DW MR data has gained increasing interest in clinical practice and research in the past years.

Diffusion MRI is challenging in many respects, and various MR sequences have been suggested to achieve optimal image quality. One fundamental challenge is the inherently low signal-to-noise ratio (SNR) of DW images, which motivates the use of MR sequences with high SNR efficiency. Another challenge is the sensitivity to motion such as that stemming from breathing and cardiac pulsation. In conjunction with the strong diffusion sensitizing gradients, motion results in unpredictable phase changes as well as echo time shifts for each acquisition. This impedes the application of multishot acquisition techniques (4) or fast spin echo sequences (5). These problems have been addressed in recent years, and promising results have been shown in particular by using multishot DWI approaches that estimate motion-related phase errors by k-space oversampling (6) or using navigators (7–9). Nevertheless, owing to their inherent robustness against motion, the vast majority of scans that are performed in practice are single-shot echo planar imaging (EPI) sequences (10).

However, single-shot EPI is susceptible to several artifacts, including global and local image distortions as well as image ghosts, which can impair the clinical value of obtained DW images and drastically limit the accuracy of quantitative diffusion (11,12) imaging. The latter requires the combination of DW images to fit a chosen diffusion model, which increases the sensitivity to encoding perturbations that result in geometrical incongruence among variable diffusion-encoded images.

One problem common to all EPI acquisition strategies is their sensitivity to gradient system imperfections. In particular, gradient delays and eddy currents cause inconsistency among the acquired k-space lines with different read direction and thus result in half–field of view ghosting artifacts. On most clinical MRI systems, this problem is addressed by EPI phase correction techniques (13). However, EPI phase correction does not account for all gradient imperfections. Moreover, gradient heating can render such calibrations invalid by altering the behavior of short–term eddy currents and mechanical oscillations.

A second challenge are eddy current field effects that are induced by the diffusion-sensitizing gradients. Because the duration of the diffusion encoding gradients is long, the resulting eddy current fields with long time

[1]Institute for Biomedical Engineering, University of Zurich and ETH Zurich, Switzerland.
[2]Laboratory for Social and Neural Systems Research, University of Zurich, Switzerland.
[3]Skope Magnetic Resonance Technologies LCC, Zurich, Switzerland.
[4]Translational Neuromodeling Unit, Institute for Biomedical Engineering, University of Zurich and ETH Zurich, Switzerland

*Corresponding author: Bertram J. Wilm, Ph.D., Institute for Biomedical Engineering, University and ETH Zurich, Gloriastrasse 35, CH-8092 Zurich, Switzerland. E-mail: wilm@biomed.ee.ethz.ch

Received 2 April 2015; revised 8 June 2015; accepted 9 June 2015
DOI 10.1002/mrm.25827
Published online 17 July 2015 in Wiley Online Library (wileyonlinelibrary.com).

constants can significantly perturb the subsequent image encoding. In the images, these effects result in distortions as well as ghosting artifacts that vary with the applied DW gradients. Eddy currents are diminished by the MR system's eddy current correction (ECC)—that is, pre-emphasis of the demand waveform that is sent to the gradient amplifier as well as demodulation of B_0 eddy currents. Another approach is to reduce eddy current effects by sequence design, such as with bipolar diffusion gradient lobes (14) or twice-refocused spin-echo sequences (15,16). The remaining eddy currents are typically addressed by coregistration after image reconstruction (17–19). However, image coregistration only addresses geometric distortions and commonly assumes an affine transformation model, which can be insufficient to model the actual image distortions. Moreover, coregistration requires sufficient SNR, which is often not available, particularly with strong diffusion encoding (high b values and/or q values).

Another source of image artifacts are drifts of the static B_0 field. Such field changes can be caused by temperature changes of the MR system's hardware components such as the shim irons or the heat shield. When the field changes are of the 0^{th} order, they result in image shifts as well as minor ghosting artifacts. Field drifts of the 1^{st} order in space result in image scaling and shearing. Except for B_0-induced ghosts, field drifts up to the 1^{st} order can potentially be addressed by the aforementioned image coregistration methods, again having to rely on high SNR in individual images. Field drifts of higher spatial order must be addressed at the image reconstruction level [eg, by static B_0 off-resonance correction (20–22)]. Such approaches, however, can only be applied when knowledge of these field changes is available.

In this study, we explore the potential of addressing field imperfections in diffusion imaging comprehensively by the recent concept of concurrent magnetic field monitoring (23–25). Field monitoring yields the actual spatiotemporal evolution of the magnetic field during image acquisition. Thus, it jointly captures eddy current effects, temperature-related field drifts, and changing behavior of the gradient system, as well as dynamic field changes of external origin. Full use of this information at the reconstruction level requires generalization of the traditional Fourier perspective such as to account for higher-order spatial encoding. A suitable algebraic strategy for this purpose was proposed recently and was shown to be effective at addressing eddy currents due to diffusion gradients (26). We now seek to evaluate the prospect of this approach from the perspective of diffusion imaging practice. To this end, we assess its benefits for typically used single-shot DW EPI sequences with a high-performing gradient system in a phantom and in vivo. Furthermore, we study the ability to compensate for thermal system drifts and imperfect gradient calibration.

METHODS

Acquisition Setup

All scans were performed on a 3T Achieva System (Philips Healthcare, Best, Netherlands) using an eight-element head receive coil array. Sixteen transmit/receive ^{19}F-based NMR probes were mounted on the surface of the head array (Fig. 1). The probe positions were chosen such as to achieve optimal conditioning for expansion into a 3^{rd}-order spherical harmonic field model. This was achieved by placing the probes in four rings with 5-6-4-1 probes per ring, respectively (27). (The coordinates of the probes are provided in the Appendix.)

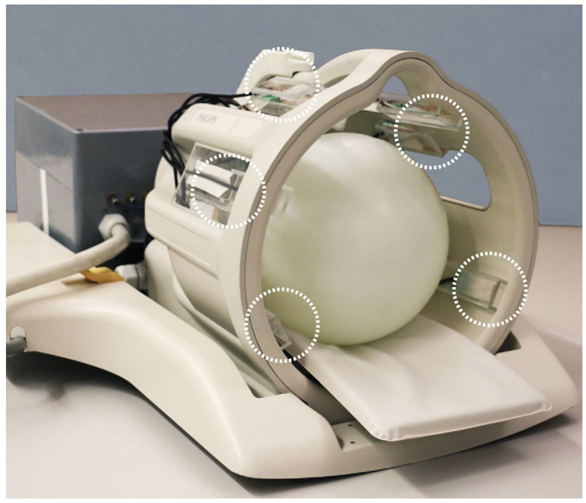

FIG. 1. Head coil array equipped with 16 ^{19}F-based transmit/receive NMR field probes. The dedicated power transmit and preamplification stages for the field probes are housed in the dark gray box in the background.

Probe excitation was triggered by the physiology trigger of the MR systems (TTL signal); a dedicated RF transmit chain was used to excite the field probes (28). The field probes' ^{19}F signals were amplified and then digitized by the MR system's spectrometer, together with the eight ^{1}H signals from the head coil array. The spectrometer was programmed to perform multiple-channel acquisition for both nuclei.

In vitro experiments were performed on a spherical phantom filled with low-diffusivity silicon oil (AK 500, Wacker Chemie AG, Munich, Germany) to minimize signal attenuation by diffusion weighting. In vivo experiments were performed in accordance with local ethics regulations on one healthy subject (female; age, 22 y) who provided written informed consent.

MR Sequence Parameters

Single-shot DW-EPI scans were acquired with a field of view of $(230\ \text{mm})^2$ and an in-plane resolution of $2.0\ \text{mm}^2$ in the phantom and $1.7\ \text{mm}^2$ in vivo in one transverse slice (thickness = 2 mm). Stejskal-Tanner (single-refocused) diffusion weighting was applied in six non-coplanar orientations $[(-2/3, -2/3, -1/3)^T$ $(-1/3, 2/3, -2/3)^T$ $(-2/3, 1/3, 2/3)^T$ $(-2^{0.5}/2, 0, -2^{0.5}/2)^T$ $(-2^{0.5}/2, 2^{0.5}/2, 0)^T$ and $(0, 2^{0.5}/2, 2^{0.5}/2)^T]$ with $b = 1000\ \text{s/mm}^2$. In addition, a b_0 ($b = 0\ \text{s/mm}^2$) reference image was acquired to obtain a full DTI dataset. SENSE undersampling by a factor of 3 was used to reduce sensitivity to B_0 off-resonance distortions and T_2* blurring. This was implemented by performing an interleaved EPI sequence with three interleaves, each of which was treated separately as a single-shot acquisition in the reconstruction. The gradient mode was set to maximum gradient strength to allow for short echo times. The echo time was 60.3 ms (in vitro) and 69.1 ms (in vivo) with a readout duration of 32 ms (bandwidth = 31.2 Hz/pixel) and 41.5 ms (bandwidth = 24.1 Hz/pixel), respectively. In vitro, two static saturation slabs were applied perpendicular to the slice to add some structure to the phantom. The number of averages was set to 9 for the in vitro scans and 27 in the in vivo scans. To allow for studying temperature-related field effects separately, gradient heating of the DW scan itself was minimized by imaging only a single slice and choosing a long repetition time (5 s).

In addition, two standard spin-warp gradient-echo data sets (resolution = 2.0 × (2.0 mm)^2, slice thickness = 4 mm, echo time = 3.6 and 3.9 ms) were acquired and used to calculate coil sensitivity and static ΔB_0 maps.

For all scans, the encoding fields were recorded using the field probes simultaneously with image acquisition. For the gradient echo scans, the field probes were excited after slice selection. In the DW scans, the field probes were excited after the diffusion-encoding gradients, since the large gradient lobes would otherwise fully dephase the field probe signal. From the probe data, a 3rd-order phase model, including the 1st-order k-space trajectory, was calculated by spherical-harmonic expansion (26) with concomitant field correction (29).

Specific Experiments

In the phantom, three DW experiments were performed. In experiment 1, the DW sequence was applied as described in the previous section. The dataset was acquired to evaluate the effect of the DW gradients on the encoding and the resulting images. In experiment 2, the above DW scan was repeated with the MR system's ECC turned off to mimic a miscalibrated or otherwise less refined gradient system. In experiment 3, experiment 1 was repeated after a gradient-intensive EPI-based functional MRI scan with a duration of 12 min that was known to heat up the MR system, to evaluate the effect of the changing MR system temperature on gradient and field drifts during a scan. The image averages were acquired in the outer loop (dynamics) of the scan such that the same contrasts were acquired in different temperature states. Experiment 3 was repeated in vivo.

Field Encoding Visualization

The unit of the phase coefficients is rad/m^N for basis functions of degree N = 0,1,2,3. Due to different spatial features and scaling factors, the coefficients per se are difficult to interpret and compare. Therefore, the phase coefficients are visualized by plotting the related maximum field excursion, in radians (rad$_{max}$), in a centered sphere of 20 cm diameter. To study the effects of the DW gradients, the phase evolution during the DW experiments was plotted after subtraction from the b_0 scan's phase coefficients. This was done for the scans with (experiment 1) and without (experiment 2) the MR system's ECC for the first two diffusion directions. To study temperature-related field effects (experiment 3), the phase evolution of the first average of the b_0 and the first two DW scans were plotted after subtraction of the relating last average that was acquired approximately 5 min later.

Image Reconstruction

All DWI datasets were reconstructed using iterative image reconstruction incorporating higher-order fields as well as coil sensitivity and ΔB_0 maps (26). The gradient echo images yielding sensitivity and ΔB_0 maps were reconstructed with the same algorithm and likewise on the basis of concurrent monitoring.

To evaluate the effect of field contributions relating to the DW gradients, the DTI data from the experiments with ECC (experiment 1) was reconstructed in four different ways:

- assuming perfect gradient behavior, based on the nominal trajectory without any correction;
- using the 0th- and 1st-order monitored trajectory from the b_0 scan (monitored b_0), but neglecting higher-order fields and DW eddy currents;
- using the 0th- and 1st-order monitored trajectory from concurrently monitored fields relating to each acquisition, to assess the remaining effect of higher-order fields; and
- using the concurrently monitored full 3rd-order phase expansions relating to each acquisition (3rd-order monitored).

To assess geometric consistency, a relative difference image between the DW and b_0 images was calculated for each of the DW images in each of the image sets. The relative difference between two magnitude images I_1 and I_2 was calculated as $2(I_1 - I_2)/(I_1 + I_2)$ for each voxel and was displayed using either a ±10% or a ±100% scale. The relative difference was set to zero where $(I_1 + I_2)$ was below a threshold near the image noise level. For the non-ECC scans (experiment 2), reconstruction and evaluation were performed similarly, but omitting the nominal reconstructions.

To assess the effect of gradient and field drift during the scan (experiment 3), all images were reconstructed using the monitored trajectory of the first average relating to each DW direction. The same reconstruction was then repeated taking measured individual B_0 shifts into account. A third set of images was reconstructed using the individually monitored 3rd-order phase expansions. Geometrical congruence and image quality were assessed by subtracting the first two sets from the individually 3rd-order monitored reconstructions. In addition, congruence between the DW images and the b_0 image was assessed for all reconstructed datasets.

For the in vivo DTI dataset, image reconstruction based on the nominal, monitored b_0 (0th- and 1st-order) and individual 3rd-order monitored trajectories was performed. Subsequently, the mean DW image, an apparent diffusion coefficient (ADC) map, a fractional anisotropy (FA) map and the color-coded FA (cFA) map were calculated for all image sets without image coregistration.

RESULTS

Observed Field Encoding

In the scans with ECC (experiment 1), the dominant phase terms during the b_0 acquisition (Fig. 2a) were the regular 1st-order (k-space) terms reflecting the EPI

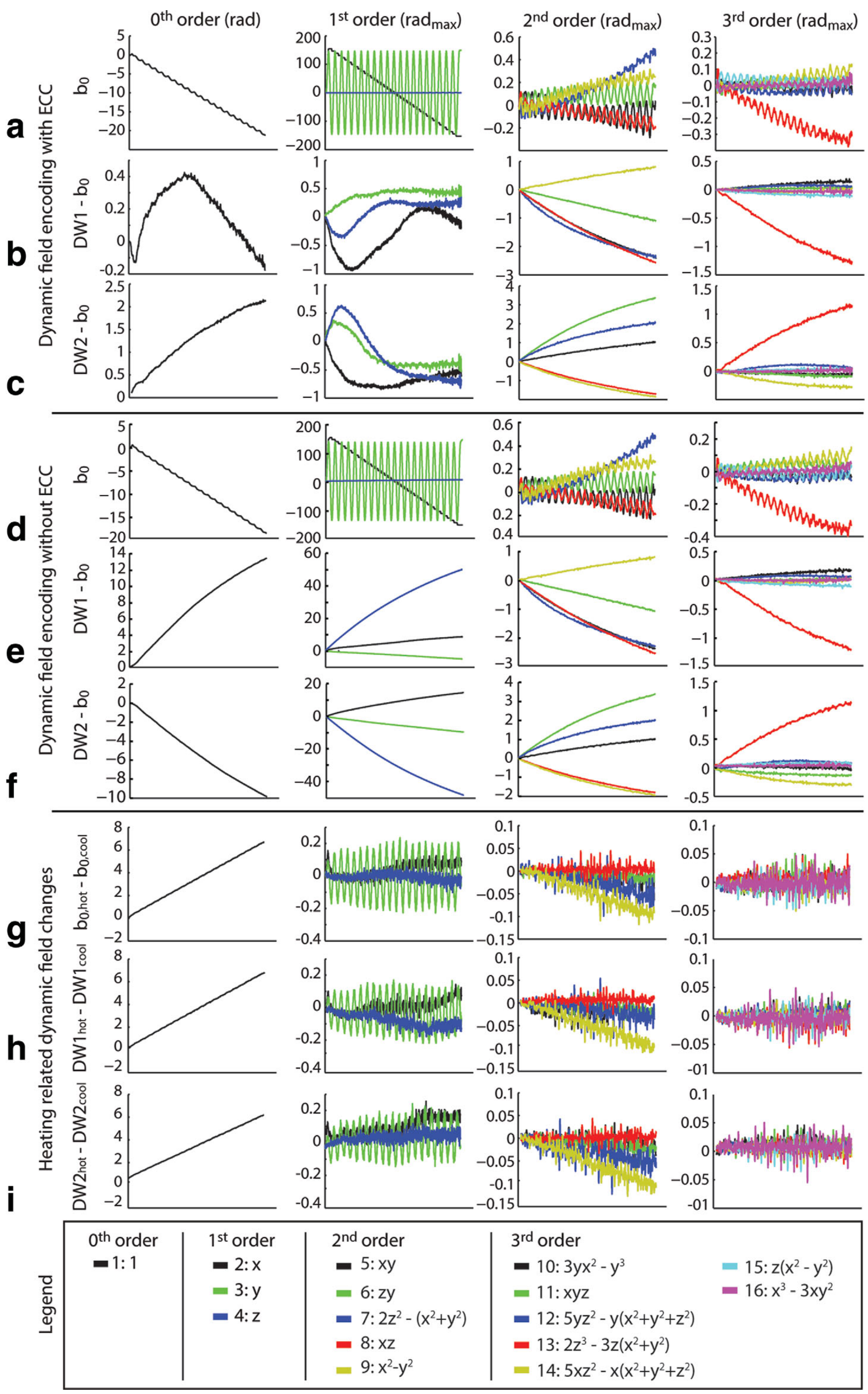

FIG. 2. Field evolution during the EPI readout separated by their spatial orders. (**a**–**c**) Scans with ECC. (**d**–**f**) Scans without ECC. Separated encoding effects of the DW gradients are shown in panels b, c, e, and f. (**g**–**i**) Difference between first (hot) and last (cool) corresponding average (dynamic) of an experiment following a gradient intensive scan plotted for the b_0 (g) and the first two DW acquisitions (h, i). Note that the *y* axis is scaled individually for each plot.

readout with only minor (<0.5 rad_{max}) contributions from higher-order terms. In addition, an approximately constant B_0 offset (linear 0^{th}-order phase) was present. When adding the DW gradients (Fig. 2b, 2c), additional 0^{th}-order deviations up to 3.5 rad as well as higher-order terms up to 3.5 rad_{max} (2^{nd} order) and 1.3 rad_{max} (3^{rd} order) were observed. The time courses of the higher-order terms indicate underlying eddy currents with noticeable decay during the readout.

In the scans without ECC (experiment 2) (Fig. 2d–2f), the apparent higher-order field terms were very similar to those with ECC (Fig. 2a–2c), as should be expected. However, the absence of the MR system's 0^{th}- and 1^{st}-order ECC resulted in strong deviations in the 0^{th}-order (20 rad) and 1^{st}-order (50 rad_{max}) terms.

Heating-related changes (experiment 3) (Fig. 2g–2i) were predominantly of 0^{th} order and consistent with slow B_0 change. Smaller differences were observed in

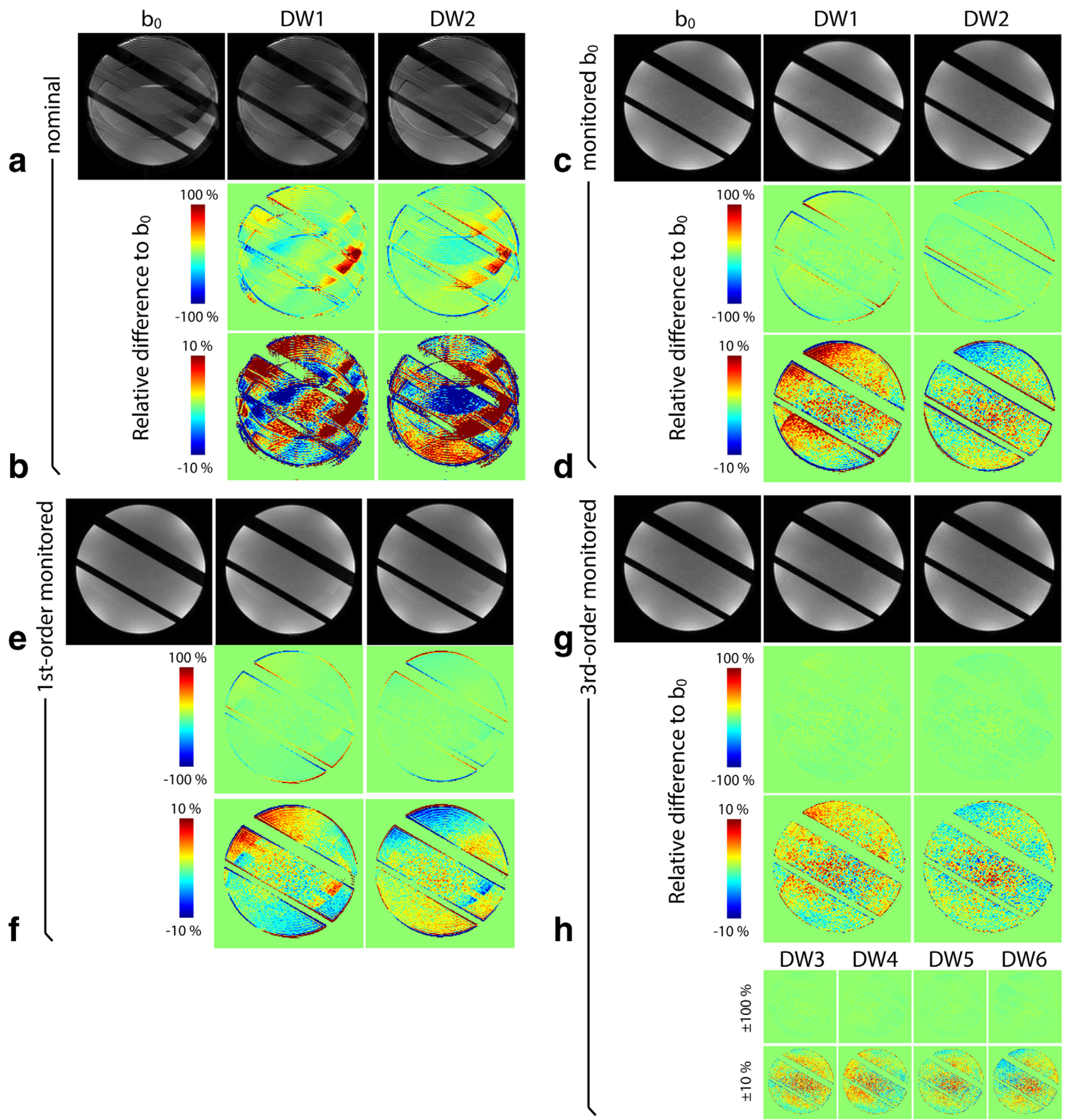

FIG. 3. Effect of encoding models on image congruence and ghost level. (**a**, **b**) Images reconstructed with nominal encoding (a) and the differences between DW and the corresponding b_0 image (b). (**c**, **d**) Images reconstructed with the monitored 1^{st}-order trajectory of the b_0 acquisition (c) and the differences between DW and the corresponding b_0 image (d). (**e**, **f**) Images reconstructed using the individually monitored 1^{st}-order encoding model (e) and the differences between DW and the corresponding b_0 image (f). (**g**, **h**) Images reconstructed using the individually monitored 3^{rd}-order encoding (g) and the differences between DW and the corresponding b_0 image (h).

the 1^{st}-order terms, particularly for the direction of the read gradient. Only minor higher-order drift was observed. The drift was very similar for the b_0 (Fig. 2g) and the DW images (Fig. 2h, 2i).

Image Reconstruction

For the scans with ECC (experiment 1), image reconstruction based on the nominal trajectory resulted in substantial ghosting artifacts (Fig. 3a) as well as image incongruence that were clearly apparent on both the full-scale and the 10% scale difference images (Fig. 3b). Reconstruction based on field monitoring during the b_0 scan (Fig. 3c) largely removed ghosting and improved the congruence among the images. However, the difference images (Fig. 3d) still indicate significant geometric inconsistency. The differences of up to 100% at the phantom edges indicate relative distortions in the order of 2/3 of a voxel size. The reconstructions using the concurrently monitored 0^{th}- and 1^{st}-order terms showed similar ghosting and distortion levels (Fig. 3e,f). Incorporation of higher-order terms (Fig. 3g) resulted in virtually exact geometrical congruence and also reduced ghosting below the level of visibility (Fig. 3h).

For the data set without ECC (experiment 2), image reconstruction based on monitoring of the b_0 scan resulted in strong relative distortion of the different DW

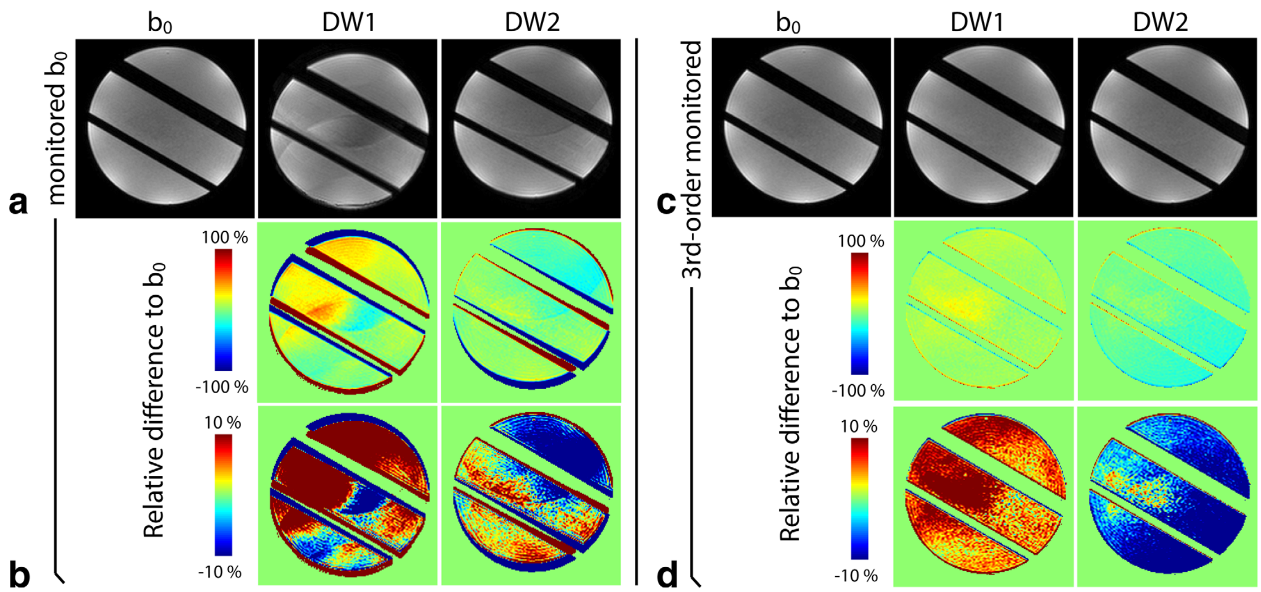

FIG. 4. (**a**, **c**) Image congruence without the MR system's ECC with (a) and without (c) concurrent field monitored reconstruction. (**b**, **d**) Differences between DW and the corresponding b_0 images.

images (Fig. 4a) and thus unacceptable variability among the DW and b_0 images (Fig. 4b). 3^{rd}-order reconstruction based on concurrently monitored field evolutions (Fig. 4c) still yielded near-perfect ghost correction and image congruence (Fig. 4d). Only an intensity difference among the DW and b_0 images and subtle geometrical inconsistency remained apparent (Fig. 4d).

The analysis of the effect of temperature drift during the scan showed that neglecting temperature-related encoding errors caused prominent ghosting artifacts (Fig. 5a) as well as shifting of the image by several pixels in the phase encoding direction (Fig. 5b). Correcting for the individual B_0 drifts (Fig. 5d) removed most of the image shifts (Fig. 5e); however, prominent image ghosting remained (Fig. 5e). In both cases, the relative differences to the corresponding b_0 scans showed that artifact levels also varied slightly depending on the diffusion encoding (Fig. 5c,f). Ghost-free images with matching geometry were obtained when reconstructing all images based on individual concurrent monitoring (Fig. 5g, 5h) indicating that these images represent the phantom faithfully.

In the in vivo dataset, reconstruction based on the nominal trajectory (Fig. 6a) resulted in visible ghosting artifacts, which were particularly noticeable in the b_0 images and the ADC map. In addition, the FA maps appeared noisy and the cFA images showed nonanatomical diffusion anisotropy throughout the brain, probably resulting from the geometrical mismatch of the DW images. Using the k-space trajectory measured during the b_0 scan (Fig. 6b) slightly improved the results, but artifacts were still apparent. Incorporation of the monitored higher-order field effects (Fig. 6c) resulted in the removal of any visible ghosts and the nonanatomical anisotropy.

DISCUSSION

In this study, the most significant field perturbations in DWI acquisitions were found to relate to eddy currents induced by the diffusion-weighting gradients, B_0 drift, and gradual changes of the short-term gradient system response during the scan. It has been demonstrated that these perturbations can be comprehensively addressed by concurrent field monitoring and algebraic image reconstruction, yielding virtually artifact-free geometrically congruent image data.

Eddy current effects caused by DW gradients had significant higher-order components not amenable to ECC. Only by higher-order reconstruction it was possible to account for the full range of field distortions. The commonly employed registration methods based on affine transformations (19) implicitly assume spatially linear and temporally constant eddy current fields. According to the findings of this study, neither of these assumptions typically hold for DWI, and thus only incomplete coregistration can be expected with affine models. Another disadvantage of image coregistration is its dependence on sufficient image SNR. This is particularly problematic for high b value and q space data. Distortion models with more degrees of freedom have been explored (30) yet arguably require even more SNR to achieve stable results. The eddy current effects observed in the present study remained largely unchanged by gradient heating and generally proved very reproducible. Therefore, image reconstruction based on prior calibration of DW eddy currents [eg, using gradient impulse response measurements (31)] may well be possible. Fast implementations of higher-order reconstruction (32), which are well suited to correct for eddy currents in DWI, may then be used to make the correction practical for clinical applications. Alternatively, image reconstruction may be accelerated by using dedicated computing hardware (33).

Slow 0^{th}-order drifts as well as changes in high-frequency 1^{st}-order fields during the scan (experiment 3) following gradient intensive scanning probably related to temperature changes in different components of the MR

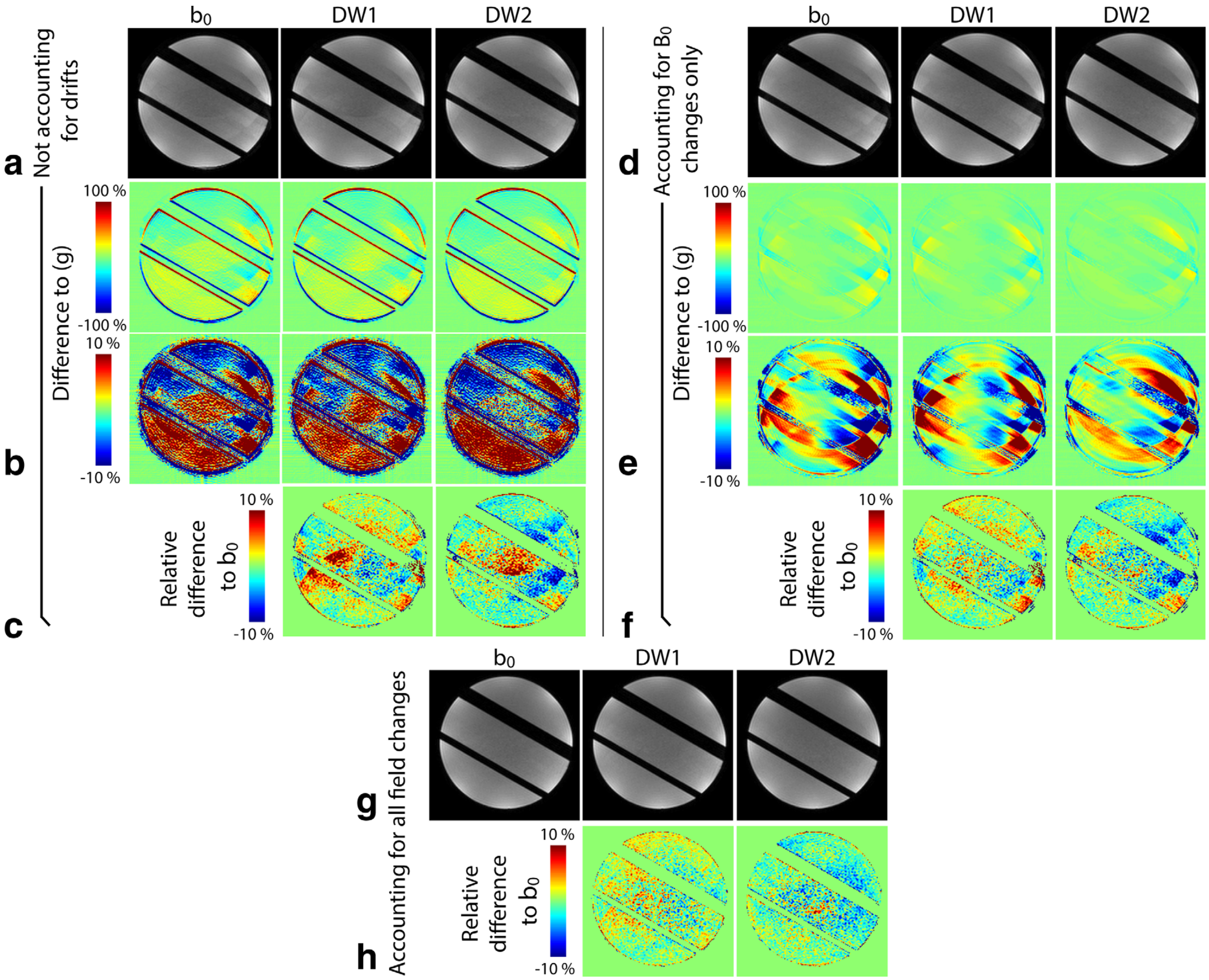

FIG. 5. Effect of field/gradient drift during the scan. (**a**) Images reconstructed when neglecting encoding changes for the individual signal averages. (**b**) Differences in the corresponding concurrently monitored images. (**c**) Differences in the corresponding b_0 image. (**d**) Images reconstructed when accounting for individual B_0 changes for all signal averages. (**e**) Differences in the corresponding concurrently monitored images. (**f**) Difference in the corresponding b_0 image. (**g**) Images reconstructed when accounting for all concurrently monitored field changes for all signal averages. (**h**) Differences in the corresponding b_0 image.

system. The analysis of the phase evolutions showed that mere correction of the slow B_0 changes was insufficient to address all artifacts in the images. The remaining ghosting artifacts could be attributed to changes in the high-frequency 1st-order encoding following gradient action, which probably relate to changes in gradient eddy currents or mechanical vibrations (34). Similar ghosting artifacts can be expected for nonmonitored scans when using pre-scan EPI phase calibration (13) during or after gradient-intensive scans. Phase reference scans embedded in the actual EPI readout (35) can partially address this problem but also prolong echo times.

By turning off the MR system's ECC (experiment 2), a miscalibrated or otherwise less refined gradient system was simulated. Even in this case, field monitoring and algebraic reconstruction achieved virtually complete ghost suppression and image congruence well below the pixel scale. Thus, the presented method may relax specification requirements on MR system/gradient hardware and its calibration. The remaining issues in this experiment were differences in image magnitude and minor residual misalignment between images with the different DW directions. They are likely related to through-plane dephasing by eddy current gradient fields in the slice direction and slight slice shifts due to strong B_0 eddy currents, respectively. The issue could be further addressed by modelling and correcting for this effect.

Similarly, concurrent field monitoring removed any visible ghosting artifacts in the in vivo DW images. Moreover, the results indicate that the achieved geometrical congruence strongly improves the quality of quantitative diffusion data in vivo, which was demonstrated by the removal of nonanatomical diffusion tensor anisotropy throughout the brain. Field monitoring also captures breathing-related field changes in head imaging, as has been reported recently (36), which probably also contributed to the achieved geometrical consistency in vivo.

Enhanced depiction accuracy and geometrical congruence hold promise for many diffusion studies. These include q-space diffusion models (12,37), investigations

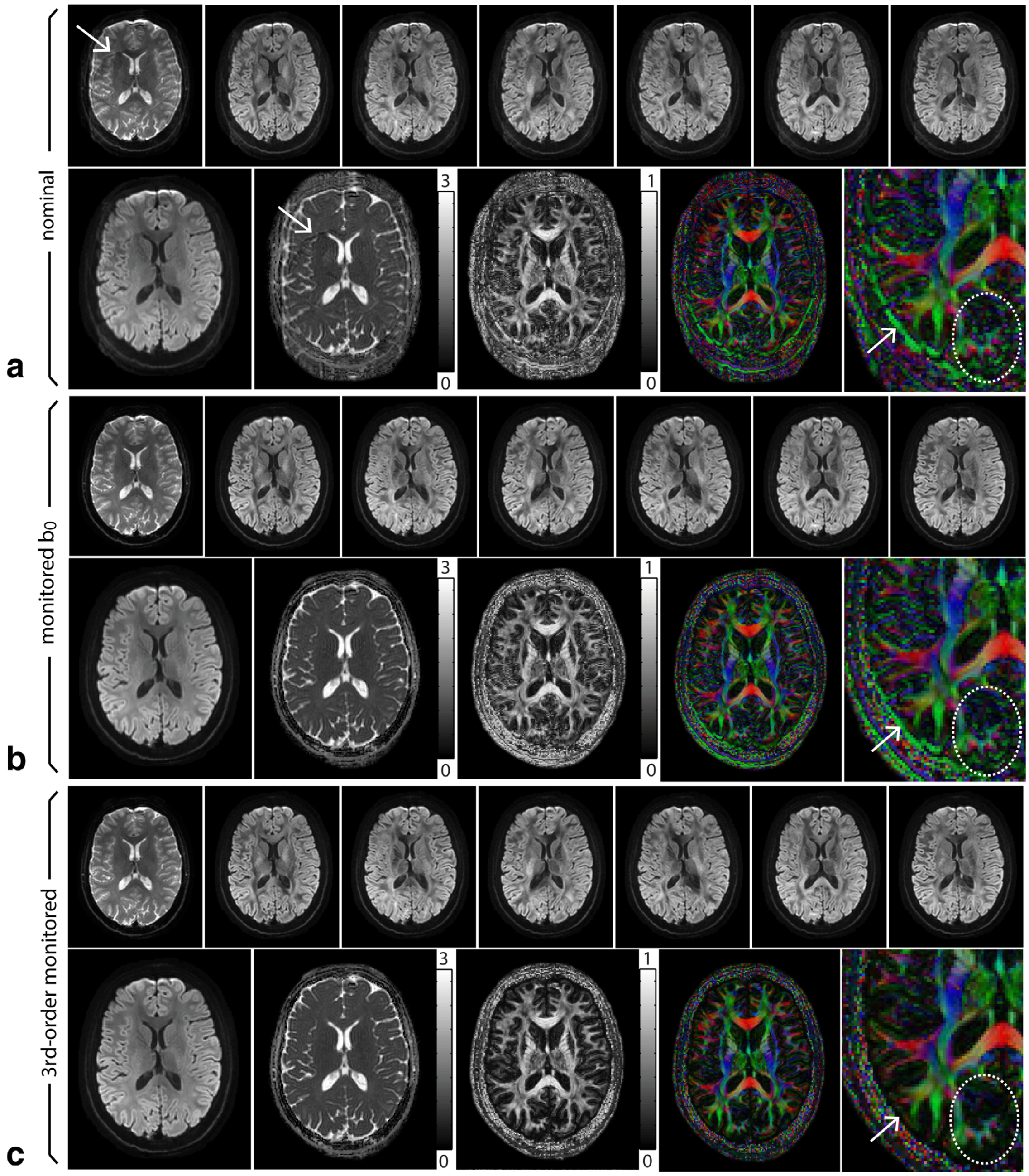

FIG. 6. In vivo DTI data reconstructed on (**a**) the nominal k-space trajectory, (**b**) the b_0 k-space trajectory, and (**c**) the concurrently monitored 3rd-order k-space trajectory. Upper row: b_0 (left) and the six individual DW directions. Lower row (left to right): mean DW image, ADC map [10^{-3}mm^2/s], FA map, cFA map, magnified cFA map. The dashed oval and the arrow in the magnified cFA images highlight noisy and increased FA values and nonphysiological anisotropy in panels a and b.

into the microstructure of grey matter (38,39), and any application that aims to investigate diffusion in the brain at high resolution (40,41).

Notably, concurrent field monitoring also improves the accuracy of parametric maps (eg, receive coil sensitivities or off-resonance maps) and their geometric consistency with data to be reconstructed with their help. Such consistency is key to the accuracy of signal models, which in turn is the basis of faithful reconstruction. Therefore, concurrent field monitoring may also prove valuable for other DWI strategies, such as multiple-shot acquisition (6,9), or more complex encoding models, such as joint estimation of parametric data (42).

APPENDIX

The field probe's positions are denoted relative to the isocenter in the nonangulated coordinate system (left–right, anterior–posterior, head–feet)^T in meters: $(0.0512, -0.1043, 0.0844)^T$, $(-0.0820, 0.0324, -0.0908)^T$, $(-0.0378, 0.1075, -0.0015)^T$, $(0.1206, -0.0352, -0.0012)^T$, $(-0.0528, -0.0671, -0.0952)^T$, $(0.0024, 0.0904, -0.0935)^T$, (0.1090,

$0.0447,\ 0.0829)^T$, $(0.0921,\ 0.0317,\ -0.0947)^T$, $(-0.1004,\ -0.0458,\ 0.0823)^T$, $(-0.0853,\ -0.0710,\ 0.0014)^T$, $(0.0007,\ 0.0022,\ -0.1547)^T$, $(0.0228,\ -0.1116,\ 0.0052)^T$, $(0.0593,\ -0.0684,\ -0.0951)^T$, $(-0.0415,\ 0.1041,\ 0.0860)^T$, $(0.0817,\ 0.0848,\ 0.0004)^T$, $(-0.1071,\ 0.0267,\ 0.0050)^T$

REFERENCES

1. Carr HY, Purcell EM. Effects of diffusion on free precession in nuclear magnetic resonance experiments. Phys Rev 1954;94:630–638.
2. Le Bihan D, Breton E, Lallemand D, Grenier P, Cabanis E, Laval-Jeantet M. MR imaging of intravoxel incoherent motions: application to diffusion and perfusion in neurologic disorders. Radiology 1986;161:401–407.
3. Moseley ME, Cohen Y, Mintorovitch J, Chileuitt L, Shimizu H, Kucharczyk J, Wendland MF, Weinstein PR. Early detection of regional cerebral ischemia in cats: comparison of diffusion- and T2-weighted MRI and spectroscopy. Magn Reson Med 1990;14:330–346.
4. Pipe JG, Farthing VG, Forbes KP. Multishot diffusion-weighted FSE using PROPELLER MRI. Magn Reson Med 2002;47:42–52.
5. Bastin ME, Le Roux P. On the application of a non-CPMG single-shot fast spin-echo sequence to diffusion tensor MRI of the human brain. Magn Reson Med 2002;48:6–14.
6. Wang F-N, Huang T-Y, Lin F-H, Chuang T-C, Chen N-K, Chung H-W, Chen C-Y, Kwong KK. PROPELLER EPI: an MRI technique suitable for diffusion tensor imaging at high field strength with reduced geometric distortions. Magn Reson Med 2005;54:1232–1240.
7. Golay X, Jiang H, van Zijl PCM, Mori S. High-resolution isotropic 3D diffusion tensor imaging of the human brain. Magn Reson Med 2002; 47:837–843.
8. Karampinos DC, Van AT, Olivero WC, Georgiadis JG, Sutton BP. High-resolution diffusion tensor imaging of the human pons with a reduced field-of-view, multishot, variable-density, spiral acquisition at 3 T. Magn Reson Med 2009;62:1007–1016.
9. Engström M, Skare S. Diffusion-weighted 3D multislab echo planar imaging for high signal-to-noise ratio efficiency and isotropic image resolution. Magn Reson Med 2013;70:1507–1514.
10. Jones DK. Diffusion MRI: theory, methods, and applications. Oxford, UK: Oxford University Press; 2010.
11. Basser PJ, Pierpaoli C. Microstructural and physiological features of tissues elucidated by quantitative-diffusion-tensor MRI. J Magn Reson B 1996:111:209–219.
12. Callaghan P. Principles of nuclear magnetic resonance microscopy. Oxford, UK: Oxford University Press; 1993.
13. Bruder H, Fischer H, Reinfelder HE, Schmitt F. Image reconstruction for echo planar imaging with nonequidistant k-space sampling. Magn Reson Med 1992;23:311–323.
14. Alexander AL, Tsuruda JS, Parker DL. Elimination of eddy current artifacts in diffusion-weighted echo-planar images: the use of bipolar gradients. Magn Reson Med 1997;38:1016–1021.
15. Reese TG, Heid O, Weisskoff RM, Wedeen VJ. Reduction of eddy-current-induced distortion in diffusion MRI using a twice-refocused spin echo. Magn Reson Med 2003;49:177–182.
16. Finsterbusch J. Double-spin-echo diffusion weighting with a modified eddy current adjustment. Magn Reson Imaging 2010;28:434–440.
17. Jezzard P, Barnett AS, Pierpaoli C. Characterization of and correction for eddy current artifacts in echo planar diffusion imaging. Magn Reson Med 1998;39:801–812.
18. Alexander DC, Pierpaoli C, Basser PJ, Gee JC. Spatial transformations of diffusion tensor magnetic resonance images. IEEE Trans Med Imaging 2001;20:1131–1139.
19. Netsch T, van Muiswinkel A. Image Registration for Distortion Correction in Diffusion Tensor Imaging, In: Gee JC, Maintz JBA, Vannier MW, eds. Biomedical Image Registration, Berlin, Heidelberg: Springer; 2003. p 171–180.
20. Noll DC, Meyer CH, Pauly JM, Nishimura DG, Macovski A. A homogeneity correction method for magnetic resonance imaging with time-varying gradients. IEEE Trans Med Imaging 1991;10:629–637.
21. Noll DC, Pauly JM, Meyer CH, Nishimura DG, Macovski A. Deblurring for non-2D Fourier transform magnetic resonance imaging. Magn Reson Med 1992;25:319–333.
22. Sutton BP, Noll DC, Fessler JA. Fast, iterative image reconstruction for MRI in the presence of field inhomogeneities. IEEE Trans Med Imaging 2003;22:178–188.
23. Barmet C, De Zanche N, Pruessmann KP. Spatiotemporal magnetic field monitoring for MR. Magn Reson Med 2008;60:187–197.
24. Barmet C, De Zanche N, Wilm BJ, Pruessmann KP. A transmit/receive system for magnetic field monitoring of in vivo mri. Magn Reson Med 2009;62:269–276.
25. De Zanche N, Barmet C, Nordmeyer-Massner JA, Pruessmann KP. NMR Probes for measuring magnetic fields and field dynamics in MR systems. Magn Reson Med 2008;60:176–186.
26. Wilm BJ, Barmet C, Pavan M, Pruessmann KP. Higher order reconstruction for MRI in the presence of spatiotemporal field perturbations. Magn Reson Med 2011;65:1690–1701.
27. Barmet C, Wilm BJ, Pavan M, Katsikatsos G, Keupp J, Mens G, Pruessmann KP. Concurrent higher-order field monitoring for routine head MRI: an integrated heteronuclear setup. In Proceedings of the 20th Annual Meeting of ISMRM, Stockholm, Sweden, 2010. p. 216.
28. Dietrich BE, Brunner DO, Wilm BJ, Barmet C, Gross S, Kasper L, Haeberlin M, Schmid T, Vannesjo SJ, Pruessmann KP. A field camera for MR sequence monitoring and system analysis. Magn Reson Med 2015. doi: 10.1002/mrm.25770.
29. Bernstein MA, Zhou XJ, Polzin JA, King KF, Ganin A, Pelc NJ, Glover GH. Concomitant gradient terms in phase contrast MR: analysis and correction. Magn Reson Med 1998;39:300–308.
30. Andersson JLR, Skare S. A model-based method for retrospective correction of geometric distortions in diffusion-weighted EPI. Neuroimage 2002;16:177–199.
31. Vannesjo SJ, Haeberlin M, Kasper L, Pavan M, Wilm BJ, Barmet C, Pruessmann KP. Gradient system characterization by impulse response measurements with a dynamic field camera. Magn Reson Med 2013;69:583–593.
32. Wilm BJ, Barmet C, Pruessmann KP. Fast higher-order MR image reconstruction using singular-vector separation. IEEE Trans Med Imaging 2012;31:1396–1403.
33. Stone SS, Haldar JP, Tsao SC, Hwu WM, Sutton BP, Liang Z-P. Accelerating advanced MRI reconstructions on GPUs. J Parallel Distrib Comput 2008;68:1307–1318.
34. Busch J, Vannesjo SJ, Barmet C, Pruessmann KP, Kozerke S. Analysis of temperature dependence of background phase errors in phase-contrast cardiovascular magnetic resonance. J Cardiovasc Magn Reson 2014;16:97.
35. Jesmanowicz A, Wong EE, Hyde JS. Phase correction for EPI using internal reference lines. In Proceedings of the 12th Annual Meeting of SMRM, New York, New York, 1993. p. 1239.
36. Vannesjo SJ, Wilm BJ, Duerst Y, Gross S, Brunner DO, Dietrich BE, Schmid T, Barmet C, Pruessmann KP. Retrospective correction of physiological field fluctuations in high-field brain MRI using concurrent field monitoring. Magn Reson Med 2015;73:1833–1843.
37. Tuch DS, Reese TG, Wiegell MR, Makris N, Belliveau JW, Wedeen VJ. High angular resolution diffusion imaging reveals intravoxel white matter fiber heterogeneity. Magn Reson Med 2002;48:577–582.
38. Nagy Z, Alexander DC, Thomas DL, Weiskopf N, Sereno MI. Using high angular resolution diffusion imaging data to discriminate cortical regions. PLoS ONE 2013;8:e63842.
39. Aggarwal M, Nauen DW, Troncoso JC, Mori S. Probing region-specific microstructure of human cortical areas using high angular and spatial resolution diffusion MRI. NeuroImage 2015;105: 198–207.
40. Miller KL, Stagg CJ, Douaud G, et al. Diffusion imaging of whole, post-mortem human brains on a clinical MRI scanner. Neuroimage 2011;57:167–181.
41. Dyrby TB, Baaré WFC, Alexander DC, Jelsing J, Garde E, Søgaard LV. An ex vivo imaging pipeline for producing high-quality and high-resolution diffusion-weighted imaging datasets. Hum Brain Mapp 2011;32:544–563.
42. Burakiewicz J, Charles-Edwards GD, Goh V, Schaeffter T. Water–fat separation in diffusion-weighted EPI using an IDEAL approach with image navigator. Magn Reson Med 2015;73:964–972.